Journal of Alloys and Compounds 804 (2019) 220–229

Contents lists available at ScienceDirect

Journal of Alloys and Compounds

journal homepage: http://www.elsevier.com/locate/jalcom

Evolution of functional properties realized by increasing laser scanning speed for the selective laser melting fabricated NiTi alloy

Y. Yang [a, *], J.B. Zhan [a], Z.Z. Sun [b], H.L. Wang [b], J.X. Lin [a, **], Y.J. Liu [c], L.C. Zhang [c]

[a] Key Laboratory of Optoelectronic Materials Chemistry and Physics, Fujian Institute of Research on the Structure of Matter, Chinese Academy of Sciences, Fuzhou, 350002, China
[b] School of Mechanical Engineering, Dongguan University of Technology, Dongguan, 523808, China
[c] School of Engineering, Edith Cowan University, 270 Joondalup Drive, Joondalup, Perth, WA, 6027, Australia

ARTICLE INFO

Article history:
Received 26 April 2019
Received in revised form
22 June 2019
Accepted 27 June 2019
Available online 28 June 2019

Keywords:
Selective laser melting
NiTi alloy
Functional properties
Martensitic transformation

ABSTRACT

The near equiatomic NiTi alloy was fabricated with selective laser melting method at a constant laser power coupled various scanning speeds from 300 mm/s to 480 mm/s. The evolution of functional properties was observed on cyclic tensile curves with emphases on the critical stress for inducing martensitic transformation and the mechanical recoverable strain. Results show that the critical stress for inducing martensitic transformation increases linearly with scanning speed, and the mechanical recoverable strain is indeed enhanced by increase of the scanning speed. Further, the highest mechanical recoverable strain of 2.29% is achieved at the applied strain of 4.5% in the sample fabricated with the highest scanning speed of 480 mm/s. The phase constitution, microstructural features and crystallographic texture were characterized in detail to interpret such evolution. It is found that the different M_s temperature and corresponding different phase constitution obtained with different scanning speed are mainly responsible for the variation of critical stress for inducing martensitic transformation and the mechanical recoverable strain. The co-existence of <111>//BD and <100>//BD crystallographic textures, as well as the variation of dislocation density show limited effect on the evolution amongst different samples.

1. Introduction

As the most important metallic shape memory material, the near equiatomic NiTi alloys fabricated by selective laser melting (SLM) method have been attracting attention. The reasons lie in the great potential for personalization design and to resolve the existing difficulties in the conventional fabrication of NiTi alloys, such as the non-accuracy control of geometric shape and high cost. Most researches were concentrated on the following topics: the fabrication optimization [1–14], the evaluation of thermo-mechanical properties [2,3,5–8,10,11] and the effect of post-heat treatments [3,5,7]. Moreover, it is noticed that the functional properties actually varies with the SLM processing parameters. These variations can be attributed to the strong sensitivity of thermo-mechanical responses relating with the martensitic transformation (MT) which depends on the chemical composition, precipitates, phase constitution, crystallographic texture and residual stress.

The influence of these factors mentioned above on the thermo-mechanical responses for SLM fabricated NiTi alloys were investigated partially by some researches. The chemical analysis on the SLM fabricated NiTi samples revealed a reduction of 0.4 wt percentage for Ni content once the higher laser power was employed [15]. Another research reported the unchanged MTTs for the SLM fabricated NiTi alloy. That was explained by the balanced Ni/Ti ratio resulting from the Ni-evaporation and precipitates formation [1,16]. As a key factor to affect the thermo-mechanical response, the difference on phase constitution for samples fabricated with different parameters is easy to be neglected [2]. Although such neglect is quite acceptable due to the serious overlap of diffraction peaks belonging to the B2 and B19' phases, the peak separation is actually necessary to identify the real phase constitution in order to interpret different thermo-mechanical responses. Concerning on the crystallographic texture, there is no clear conclusion till now because both <100> [4,5] and <111> [17] orientations parallel to

* Corresponding author.
** Corresponding author.
E-mail addresses: yy@alum.imr.ac.cn (Y. Yang), franklin@fjirsm.ac.cn (J.X. Lin).

https://doi.org/10.1016/j.jallcom.2019.06.340
0925-8388/

the building direction (BD) were reported. What is more, the variation of several variables at the same time including the laser power, scanning speed and hatch spacing were introduced for most researches, which also bring difficult for further clarification the influence on the thermo-mechanical responses.

Indeed, a near equiatomic NiTi alloy has already been successfully fabricated by SLM method in our recent work [18]. The MT relating with the thermo-mechanical responses were characterized by the martensitic start phase transformation temperature (M_s) and the critical stress inducing martensitic transformation (σ_c). It was clearly highlighted that the Clausius-Clapeyron equation can be respected only by changing the scanning speed while keeping the laser power constant. This conclusion makes it possible to obtain targeted σ_c and M_s values by adjusting the manufacturing parameters on the one hand. Further, it also implies that the variation of functional properties would probably occur with increasing the scanning speed. Therefore, questions about how and why the functional properties vary under the circumstance arise. The investigation on these questions are of importance because, on the one hand, they can shed new insights into the physical metallurgical understanding of the SLM fabrication, and on the other hand, these questions inspire hints for fulfillment of potential more complex fabrication on the basis of shape memory alloys.

To verify the variation of functional properties and explore the underlying mechanisms, the NiTi alloy samples fabricated with a constant laser power coupled a series of different scanning speeds were symmetrically evaluated with cyclic tensile test. The electron backscattered diffraction (EBSD) mapping and transmission electron microscopy (TEM) were conducted to reveal the microstructural characteristics. The XRD and DSC were used to identify the phase constitution. The XRD textures were measured to analyze the crystallographic orientation. From these results obtained, the mechanisms for variation of functional properties were discussed.

2. Materials and methods

The near equiatomic NiTi alloy powder were produced through electrode induction-melting gas atomization (EIGA) with the $Ni_{59.68}Ti_{40.32}$ (wt. %) ingot by AMC Powders Metallurgy Technology Company (Beijing, China). The chemical composition of the powder was shown in Table 1. The elemental contents of titanium, nickel and iron were measured by inductively coupled plasma-atomic emission spectroscopy (ICP-AES). The content of oxygen was determined by infrared method after fusion under inert gas. The content of carbon was measured by high frequency combustion method with infrared measurement. The size distribution of the powder particles ranges from $D_{10} = 24.1$ μm to $D_{90} = 54.9$ μm that accords with a Gaussian distribution centered on $D_{50} = 40.6$ μm. The phase constitution of the powder was revealed as only B2 phase. The commercial SLM machine of Mlab-R (Concept Laser) was used to fabricate samples under the protection of argon atmosphere (99.99%) with a constant oxygen content of 300 ppm.

Regarding the fabrication process, the laser power (P), hatch distance (h) and layer thickness (t) were kept constant at 60 W, 110 μm and 25 μm, respectively, while the scanning speed (v) was varied from 300 mm/s to 480 mm/s. Therefore, according to the equation of $E = P/(v \times h \times t)$ [19–21], the value of E, which represents the delivered laser beam energy per volume of material (energy density) during the selective laser melting process can be calculated and shown with all parameters in Table 2. The samples were hereafter labeled as 60W-x, which indicates that the sample was produced with the scanning speed of x mm/s. Further, a meander pattern was used as the scanning strategy to reduce the thermal stress within layers, while the scanning angle was alternated by 90° upon the precedent layer to minimize the thermal stress between layers. The control and optimization of the SLM fabrication process are performed firstly via maximizing density on the basis of the Archimedes' principle. This process has been done at least three times for each sample and all the processing conditions lead to a relative density higher than 99.5%.

Table 1
The chemical composition of the as-received NiTi alloy powder.

Element	Ti	Ni	O	Fe	C
Wt. %	44.48	55.98	0.046	0.004	0.0025

Cubic specimens with a size of 10 mm × 10 mm × 10 mm were deposited directly on the NiTi substrate for microstructural characterization, phase and texture analysis. Normalized flat tensile specimens with 5 mm × 20 mm × 2 mm gage dimensions were also deposited in one single fabrication process. The sample coordinate system was defined with building direction (BD), normal direction (ND) and transverse direction (TD) (see Fig. 1). This coordinate would be used for both the EBSD analyses and the XRD texture analyses. The tensile direction was chosen to be parallel to the TD direction. All specimens were mechanically polished about 100 μm in order to remove defects on the rough surface before testing. Functional properties were estimated by cyclic tensile tests with a strain rate of 10^{-3} s^{-1} on the INSTRON 3369 machine. Cyclic tensile tests were conducted with a strain increments of 0.5% followed by stress release up to applied strain of 6%. An extensometer was used to ensure the accuracy of strain.

A Netzsch DSC 200 F3 DSC with a heating/cooling rate of 10 °C/min in nitrogen atmosphere were used to estimate the characteristic temperatures for phase transformation from −60 °C to 80 °C. The XRD was performed at ambient temperature for phase constitution on Rigaku D-Max 2400 in the 2θ angle range of 35–80° with a scanning step of 0.01°. Texture analysis based on X-ray diffraction were conducted on an X'pert pro system with Cu-K_α radiation ($\lambda = 0.154060$ nm). The step size used for the data acquisition was settled as 5° for both Phi and Psi angles. For texture analysis, the sample coordinate system BD-ND-TD was used. Pole figures (PFs) of $\{110\}_{corr}$ and $\{200\}_{corr}$ were corrected with the raw data of three most important pole figures {110}, {200} and {211} after applying corrections of background and defocusing.

The microstructural characterization were performed with the EBSD analyses in the FEI NanoSEM450 field-emission SEM equipped with a NordlysMax2 EBSD detector. The samples were prepared by electrolytic polishing at 25 °C in a solution composed of 6% $HClO_4$ acid and 94% CH_3OH in volume. Further TEM observations were conducted using a JEOL 2100 operated at 200 kV. Thin foils for TEM observations were cut as disks of 3 mm in diameter, further mechanically polished to a thickness of 60 μm and then thinned by a twin-jet electro-polishing technique with a solution composed of 80% CH_3OH and 20% H_2SO_4 solution in volume. Twin-jet electropolishing was stopped before perforation and the samples were finally thinned by ion milling with a Fischione 1010 Model.

3. Results and analysis

3.1. Microstructural observation

The optical microstructures of the SLM fabricated samples were observed on the side plane in our previous investigation [18]. Due to epitaxial growth of grains during the SLM process, all microstructures display similar columnar grains along the building direction that accords well with other references [1–4]. There are no obvious defects like the gas pores or impurities. With increasing the scanning speed from 300 mm/s to 480 mm/s, no distinct difference

Table 2
The processing parameters for selective laser melting of the NiTi alloy.

Number	Power, (W)	Scanning speed (mm/s)	Hatch spacing (mm)	Layer thickness (μm)	Energy intensity (J/mm^3)
60W-300 mm/s	60	300	110	25	72.73
60W-320 mm/s	60	320	110	25	68.18
60W-335 mm/s	60	335	110	25	65.13
60W-360 mm/s	60	360	110	25	60.61
60W-380 mm/s	60	380	110	25	57.42
60W-410 mm/s	60	410	110	25	53.22
60W-440 mm/s	60	440	110	25	49.59
60W-480 mm/s	60	480	110	25	45.45

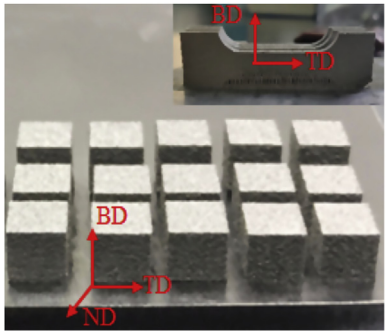

Fig. 1. Morphology of SLM fabricated cubes and tensile test samples in which the BD, ND and TD represents the building direction, normal direction and transverse direction, respectively.

on the grain size or defects can be observed amongst all samples.

The EBSD analyses were then conducted to explore more microstructural information. Relevant results on three selected samples 60W-300 mm/s, 60W-360 mm/s and 60W-480 mm/s were presented in Fig. 2a and b, 2c and 2d, 2e and 2f, respectively, in terms of inverse pole figure (IPF) mapping. The EBSD results in Fig. 2 for all samples were indexed with lattice information of the B2 phase.

The black arrows on the Fig. 2e and f indicate the external sample coordinate defined with BD, TD and ND. The IPFs-BD in Fig. 2a, c and 2e show checkerboard pattern on TD-ND plane, but the IPFs-BD in Fig. 2b, d and 2f show columnar morphology on TD-BD plane. As early mentioned, the grain size and more details cannot be noticed from the optical microstructures. But with EBSD, one can find that the boundaries of columnar grains are significantly overlapped in the sample 60W-300 mm/s compared to the other two samples, as evidenced by two parallel white lines on the TD-ND planes. This is also supported by comparing the morphologies on the TD-BD planes, as shown by the wider gaps marked by two parallel black lines between columnar grains for sample 60W-480 mm/s (Fig. 2f) than sample 60W-360 mm/s (Fig. 2d), but no such gap can be observe in 60W-300 mm/s (Fig. 2b). These gaps were well indexed in Fig. 2a, c and 2e. Reasons can be attributed to that the gap between columnar is actually composed of large quantity of sub-grain boundaries and dislocations which is more visible on the TD-BD plane, thereby affecting the indexation rate on the TD-ND plane.

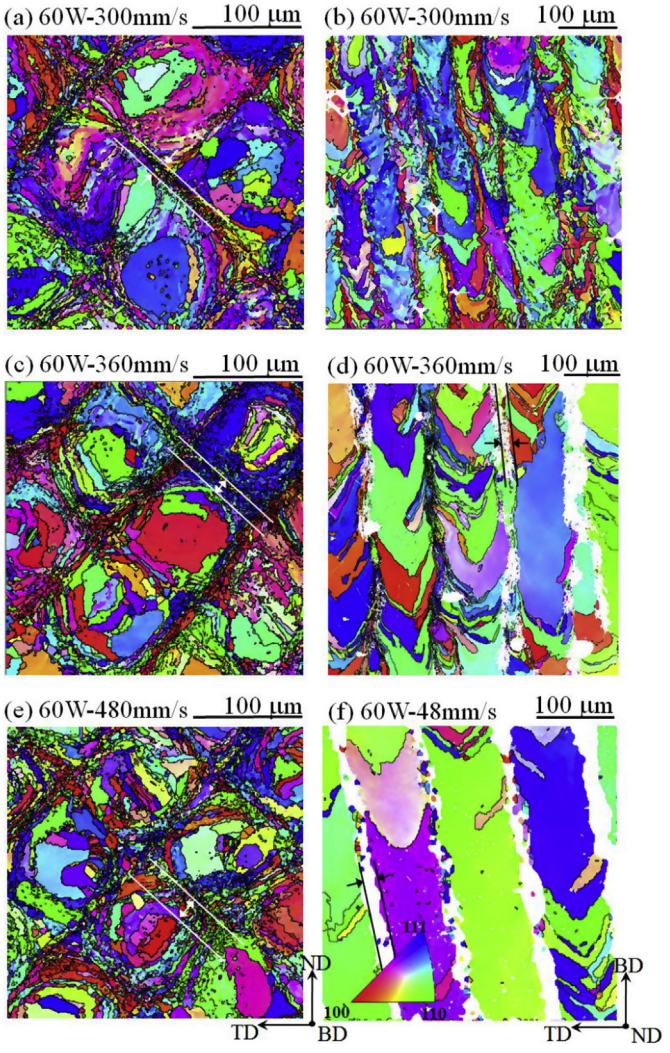

Fig. 2. EBSD Mapping on the NiTi alloy samples fabricated with a laser power of 60 W, a hatch spacing of 110 μm and a layer thickness of 25 μm, but with different scanning speeds. The BD, ND and TD represents the building direction, normal direction and transverse direction, respectively.

3.2. Phase constitution

Fig. 3 displays the whole XRD spectrums in the angle range of 35–80° for all samples. Three main peaks (110) $_{B2}$, (200) $_{B2}$ and (211) $_{B2}$ belonging to B2 phase are indicated by black solid dots in Fig. 3a besides the B19′ martensitic peaks indicated by red solid dots. With increasing the scanning speed from 300 mm/s to 480 mm/s from the lower to the upper area, the relative intensity of diffraction peaks for B19′ phase is reduced and the peak width for B2 phase becomes narrower. Especially for the samples fabricated with scanning speed higher than 360 mm/s, it seems that nearly no B19' martensite can be observed.

In order to precisely distinguish the evolution of phase constitution with increasing the scanning speed, the peak separation and fitting were performed on the partial spectrums in the angle range of 35–50° around the main (110) $_{B2}$ peak where the most intense

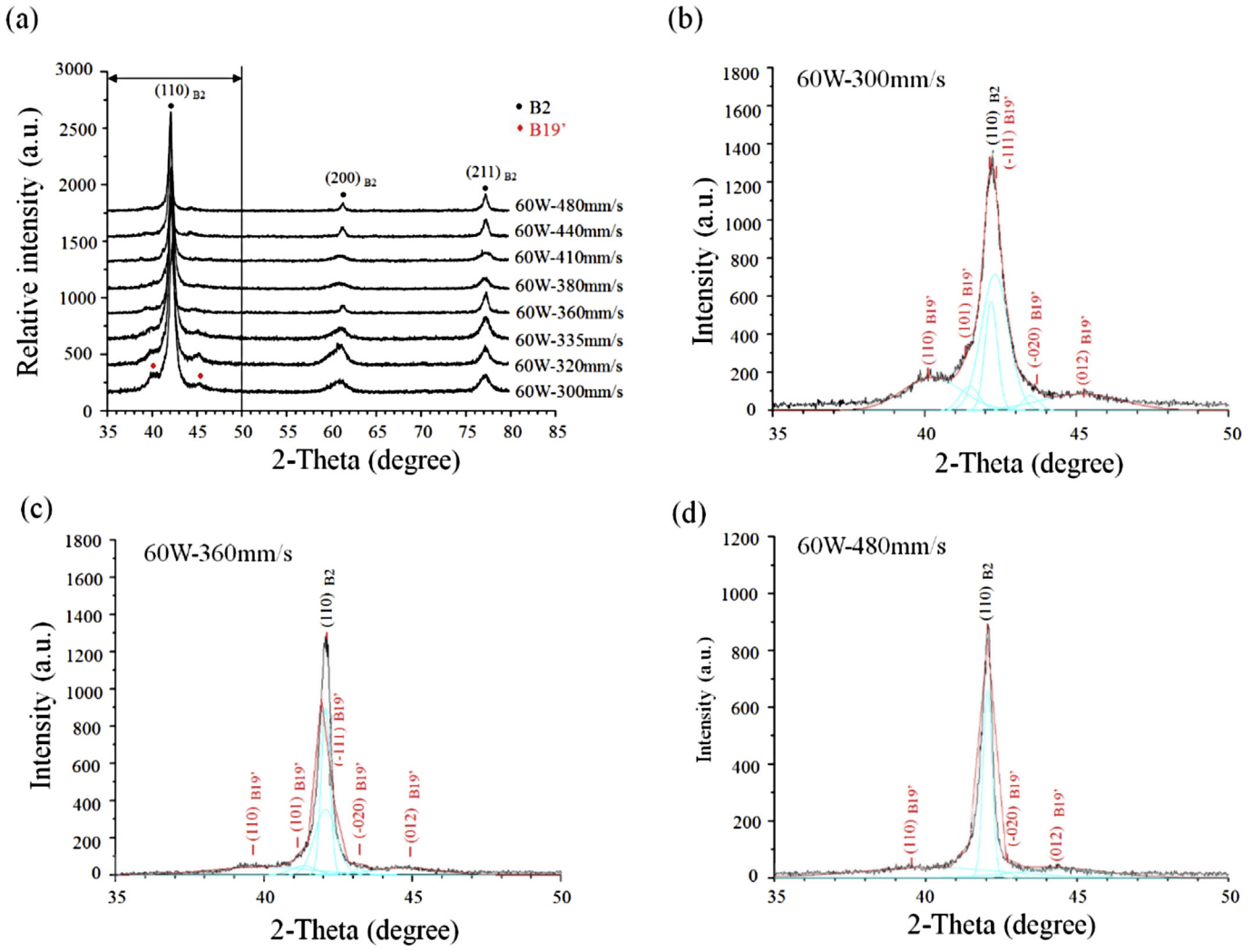

Fig. 3. (a) The whole XRD spectrums for all samples and peak fitting around the main $(110)_{B2}$ peak for selected samples: (b) 300 mm/s, (c) 360 mm/s and (d) 480 mm/s.

peaks are present. Relevant results on the sample 60W-300 mm/s is presented in Fig. 3b. As seen from the Fig. 3b, diffraction peaks of $(110)_{B19'}$, $(101)_{B19'}$, $(-111)_{B19'}$, $(020)_{B19'}$, $(012)_{B19'}$ are clearly visible and highlighted separately in blue. Based on these separated peak, the Gaussian fitting was done and fitted spectrum was highlighted in red, which is well matched with the obtained spectrum. Similar results on the samples 60W-360 mm/s and 60W-480 mm/s are shown in Fig. 3c and d, respectively. The intensity of diffraction peaks belonging to B19′ phase decreases or even vanishes with increasing the scanning speed. Therefore, the NiTi samples fabricated with laser power of 60 W is composed of both B2 and B19′ phases when the lower scanning speed was adopted. But the volume fraction of B19′ phase becomes less with increasing scanning speed from 300 to 480 mm/s. When the scanning speed is as higher than 480 mm/s, the volume fraction of B19' phase can be nearly ignored.

3.3. Crystallographic texture

On the basis of XRD spectrums shown in Fig. 3, the crystallographic texture were measured. Three main peaks of $(110)_{B2}$, $(200)_{B2}$ and $(211)_{B2}$ for the three samples 60W-300 mm/s, 60W-360 mm/s and 60W-480 mm/s were chosen for data collection in the Euler cradle. According to the raw data, the corrected pole figures (PFs) of $\{110\}_{corr}$ and $\{200\}_{corr}$ were calculated and are presented in Fig. 4. The horizontal and vertical directions in the PFs are parallel to the TD and BD directions which coincide with the sample coordinate. In Fig. 4a for sample 60W-300 mm/s, five most intensive {110} poles can be observed. Combining with the three most intensive {100} poles, the {1−10}<11−1> texture is identified and highlighted with solid square symbols. This means that the BD for sample 60W-300 mm/s shows a preferential orientation of along <111> direction for B2 phase which was reported by others in the SLM fabricated NiTi alloy [17].

For the sample 60W-360 mm/s, the PFs in Fig. 4b shows similarity contours with the sample 60W-300 mm/s in Fig. 4a. Hence, the texture of <111>//BD also exists. But the most intensive {200} poles indicate the co-existence of another additional texture <100>//BD highlighted with solid black triangles symbols. The preferential orientation of <100> parallel to the BD is deemed as the most efficient channel for heat dissipation and therefore was commonly observed in SLM fabricated cubic alloys including NiTi alloy [4,5], CoCr [22,23], Al [24], Ni [25], Ti6Al4V [26] alloys. For the sample 60W-480 mm/s, the PFs in Fig. 3c also reveals the co-existence of <111>//BD and <100>//BD textures although the intensity of the <100>//BD seems reduced.

Therefore, it can be concluded that the fiber texture of <111>// BD is formed in all these three samples but the fiber texture of

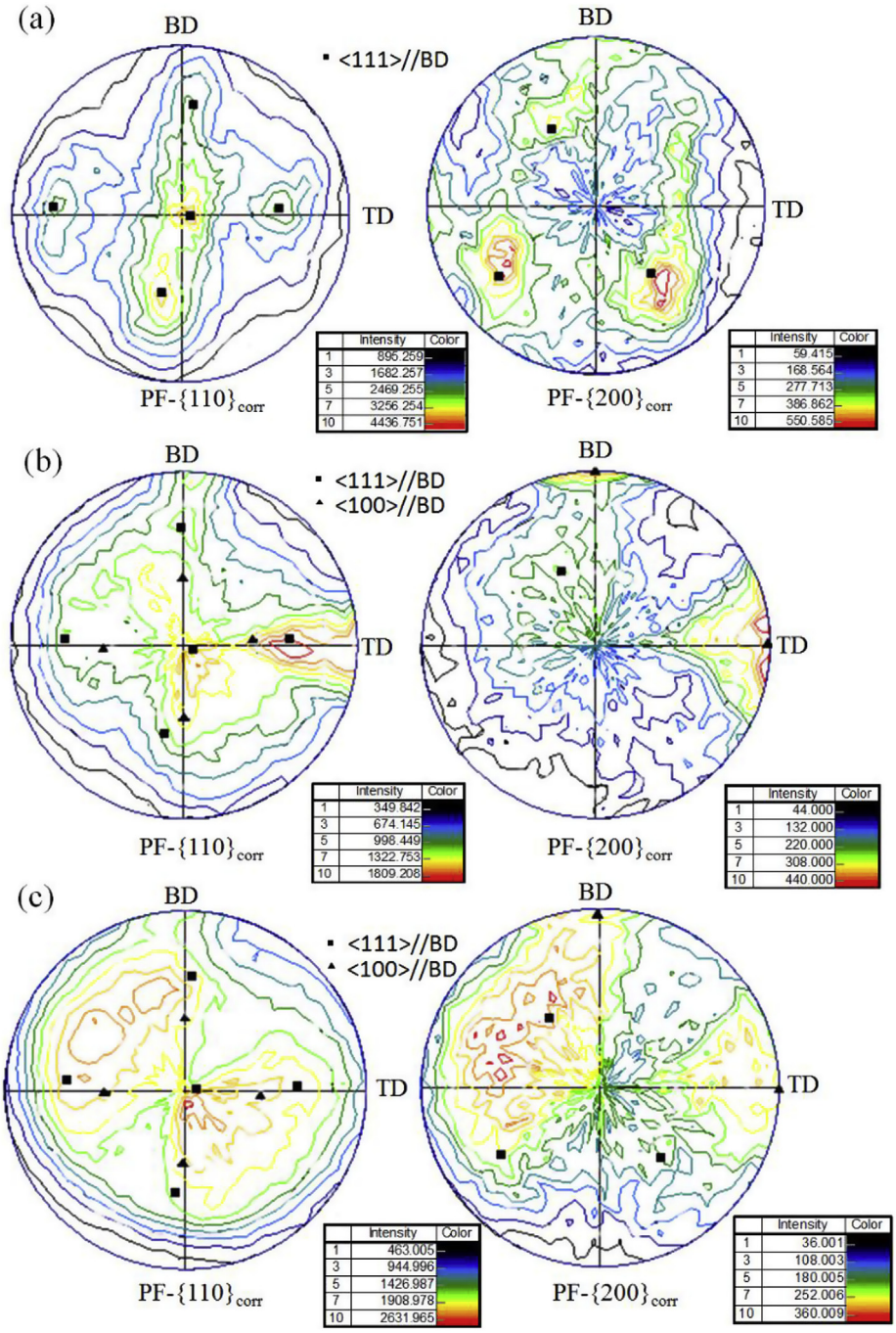

Fig. 4. The corrected pole figures of $\{110\}_{corr}$ and $\{200\}_{corr}$ for the samples fabricated with different scanning speeds: (a) 300 mm/s, (b) 360 mm/s and (c) 480 mm/s.

<100>//BD only appears at higher scanning speed. Further, the contour lines become less aggregated with increasing the scanning speed. This phenomenon hints the higher scanning speed leads to a more discrete distribution of crystallographic orientation and thus the texture is weakened with increasing the scanning speed.

3.4. DSC analysis

The DSC experiments were conducted on all samples and relevant results are shown in Fig. 5. On the DSC curves in Fig. 5a, the characteristic temperatures including martensite start (M_s), martensite finish (M_f), austenite start (A_s) and austenite finish (A_f) temperatures [27] used to characterize the martensitic transformation between the B2 and B19' phases can be measured with the intersection method of two tangent lines as shown in Fig. 5a. The room temperature of 25 °C is highlighted by a vertical dash line. Another two important temperatures M_p and A_p correspond to the maximum and minimum heat flow on cooling and on heating, respectively. All these obtained characteristic temperatures were recorded and then plotted in relationship with the scanning speed in Fig. 5b.

With increasing the scanning speed, all these characteristic temperatures show a decreasing tendency in Fig. 5b. This means that the higher scanning speed entirely suppresses the transformation between B2 phase and B19′ phase to lower temperature range. Therefore, the stability of B2 phase is enhanced on the

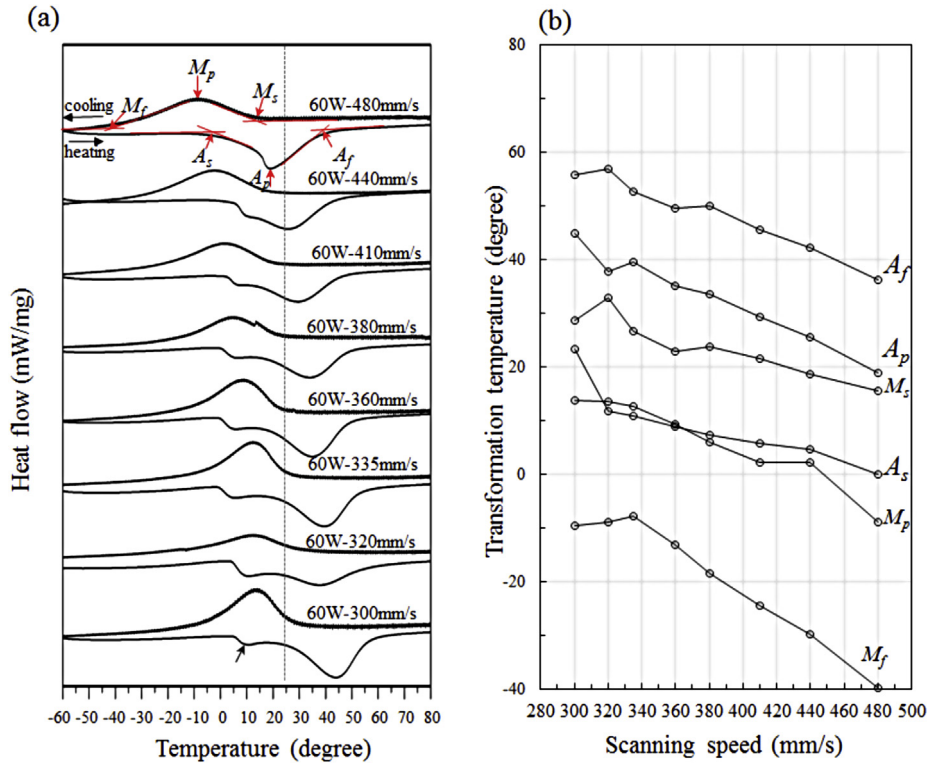

Fig. 5. DSC curves of all SLM fabricated samples in which the M_s, M_f, A_s and A_f represents martensite start, martensite finish, austenite start and austenite finish temperatures, respectively. The M_p and A_p represents the temperature corresponding to the maximum and minimum heat flow on cooling and on heating, respectively. The room temperature was marked by a vertical dash line.

condition of higher scanning speed. Further, it should be noticed that M_s temperatures are almost lower than the room temperature for all cases. This can be linked with the phase constitution analyzed from XRD spectrum. As for the SLM fabricated NiTi samples, they experienced an extremely fast cooling process after melting under high energy of laser beam, the accurate temperature for B19′ martensite to nucleate corresponds to the M_s value. Once the M_s temperature is lower than the room temperature, it is impossible to form the B19′ martensite. For the 60W-300 mm/s sample, the M_s temperature is slightly higher than the room temperature, small quantity of B19′ phase is reasonable to be detected in XRD spectrum in Fig. 3b. However, for samples fabricated with scanning speed of 360 mm/s, the M_s temperature seems to coincide with the room temperature, so very few B19′ phase are observed in Fig. 3c. But for the samples fabricated with scanning speed of 480 mm/s, the M_s temperature is indeed lower than the room temperature; this is the reason why nearly no B19' phase is detected in Fig. 3d. It is still interesting to note that there are some small shoulder peaks on the heating curves, as indicated by black arrows in Fig. 5. Such shoulder peaks can be ascribed by the inhomogeneous microstructure which leads to the elemental partition during the SLM process [28].

3.5. TEM observations

The TEM observations on samples 60W-300 mm/s, 60W-360 mm/s and 60W-480 mm/s are shown in Fig. 6a–c, 6d-6f and 6g-6i, respectively. The bright field images (BFIs) in Fig. 6a and b shows the typical morphologies of sample 60W-300 mm/s in which the grain size is measured between 300 and 500 nm. Dense dislocation tangle is also observed in Fig. 6b. The selected area diffraction pattern (SADP) indexed to be B2 phase from the zone axis of $[-1-10]_{B2}$ is obtained from the specific area circled in white in Fig. 6a. However, the martensitic B19′ phase is not detected in several different selected areas. One reason can be due to the well-known spontaneous strain relaxation occurring during the preparation of the thin TEM specimens [29,30] and consequently the B19' phase could have been transformed back to the B2 phase.

Regarding the sample 60W-360 mm/s, the BFIs in Fig. 6d and e reveal the hint of B19′ plate showing needle-like morphology on the B2 matrix as pointed by red arrows in the BFIs. The corresponding SADP in Fig. 6f from the zone axis of $[010]_{B19'}$ is obtained from the area circled by white in Fig. 6e. For the sample 60W-480 mm/s, typical morphology in Fig. 6g and h also reveals the existence of B2 phase identified by the SADP from the zone axis of $[100]_{B2}$ in Fig. 6i. Except the vanishment of B19' phase due to spontaneous strain relaxation, the difference amongst these three selected samples lies in the grain size and dislocation density. It is evidenced that the sample fabricated with lower scanning speed of 60W-300 mm/s shows smaller grains size and higher dislocation density. This contributes to some extent to the wider diffraction peaks in the XRD spectrum for the sample 60W-300 mm/s. However, the dislocation density in the SLM fabricated samples is not as high as in the cold deformed NiTi alloys.

3.6. Cyclic tensile testing

Fig. 7 presents the cyclic tensile curves consist of strain increment of 0.5% followed by stress release up to the final applied strain of 6.0% for all NiTi alloy samples. Each curve displays a stress plateau due to the martensitic transformation and hysteresis loops between loading and unloading. The stress plateau results from the reorientation martensitic plates and reversible stress-induced martensitic transformation. In general, it can also be noticed that

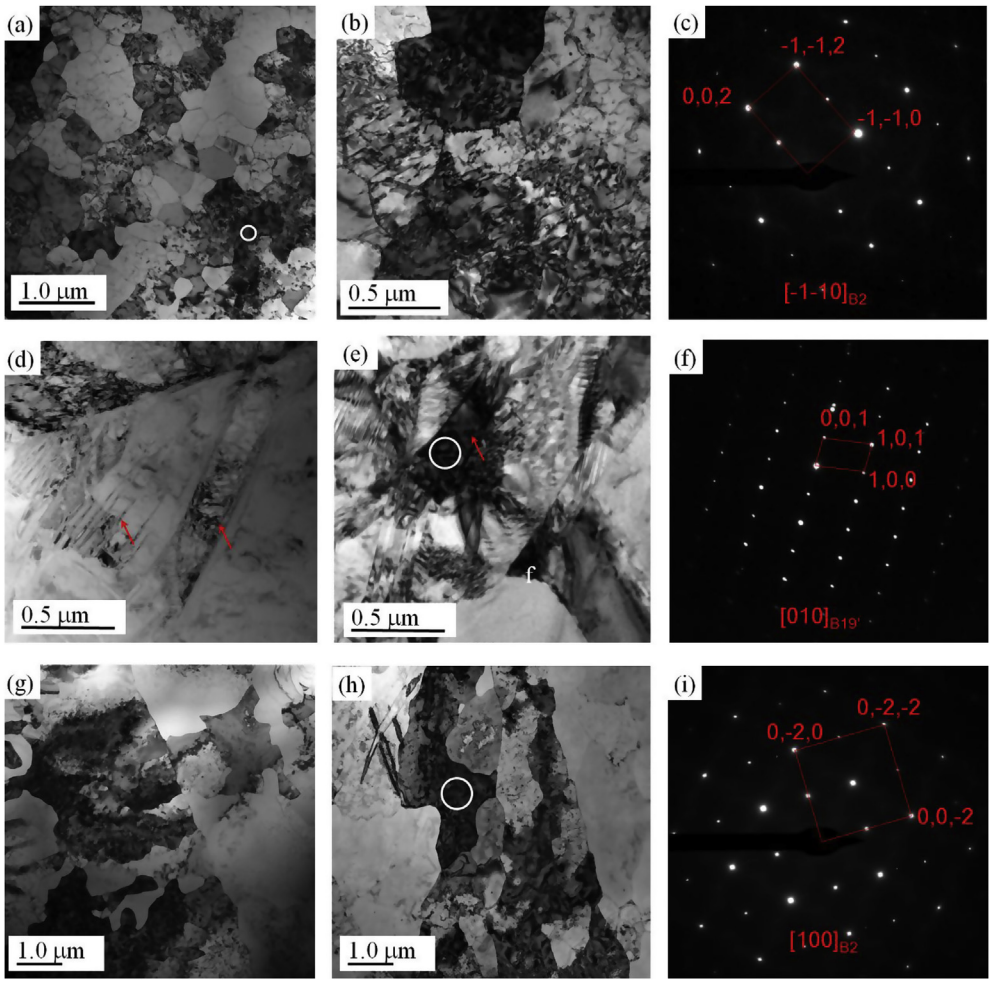

Fig. 6. TEM observations on SLM fabricated NiTi alloy samples (a–c) 60W-300 mm/s, (d–f) 60W-360 mm/s, (g–i) 60W-480 mm/s: (a) BFI showing small grains, (b) BFI showing dislocation tangles, (c) SADP obtained from the area highlighted by white circle in (a), (d, e) BFIs showing martensitic plates marked by red arrows, (f) SADP obtained from the area highlighted by white circle in (e), (g, h) typical BFIs and (i) SADP obtained from the area highlighted by white circle in (h). (For interpretation of the references to colour in this figure legend, the reader is referred to the Web version of this article.)

the area of hysteresis loop becomes larger when a higher scanning speed is employed.

Two important values that are initial yielding stress corresponding to the critical stress inducing martensitic transformation (σ_c) and the mechanical recoverable strain (ε_{rec}), were measured for evaluation of the functional properties. The method via the intersection method of two tangent red lines to measure the former value of σ_c is shown in Fig. 7a. The value of σ_c for each sample was then plotted with respect to the scanning speed in Fig. 8a. Concerning on the evaluation of the ε_{rec}, each cycle on the cyclic tensile curves composed of loading process to a certain applied strain followed by stress release was separately analyzed. The ε_{rec} was then calculated as the difference value between the applied strain (ε_t) and residual strain (ε_{res}) as shown in Fig. 7h. The results were plotted as a function of the applied strain in Fig. 8b.

It can be observed in Fig. 8a that the critical stress is observed to increase linearly with respect to scanning speed. That is because the critical stress actually depends on the difference between M_s and testing temperature [30], where the M_s indeed decreases linearly with increasing the scanning speed as revealed in Fig. 5b. The linear fitting process has been performed and the slope of 0.97 MPa/mm.s^{-1} was obtained. The evolution of mechanical recoverable strain with variation of applied strain and scanning speed is shown in Fig. 8b, from which it can be seen the highest recovery recoverable strain of 2.29% was obtained for the sample 60W-480 mm/s at applied strain of 4.5%. Additionally, the mechanical recoverable strain generally shows a linear increase in the beginning, then is followed by a non-linearity transition and finally ends up with a stabilized plateau for all samples. However, such evolution differs amongst different samples.

4. Discussion

4.1. Functional properties relating with martensitic transformation

According to the phenomenological theory of martensitic crystallography (PTMC), the functional properties for NiTi alloy are linked with the martensitic transformation in terms of crystallographic shear between the austenitic B2 phase and martensitic B19' phase [30]. Therefore, the functional properties in this present study were characterized from the viewpoints of both stress and strain by the critical stress for inducing martensitic transformation and mechanical recoverable strain, respectively. As displayed in Fig. 7, the two values were measured with cyclic tensile test at room temperature and were plotted with respect to the scanning speed as shown in Fig. 8 for further evaluation of the functional properties depending on the SLM fabricated parameters.

Seen from Fig. 8a, the critical stress increases linearly with the

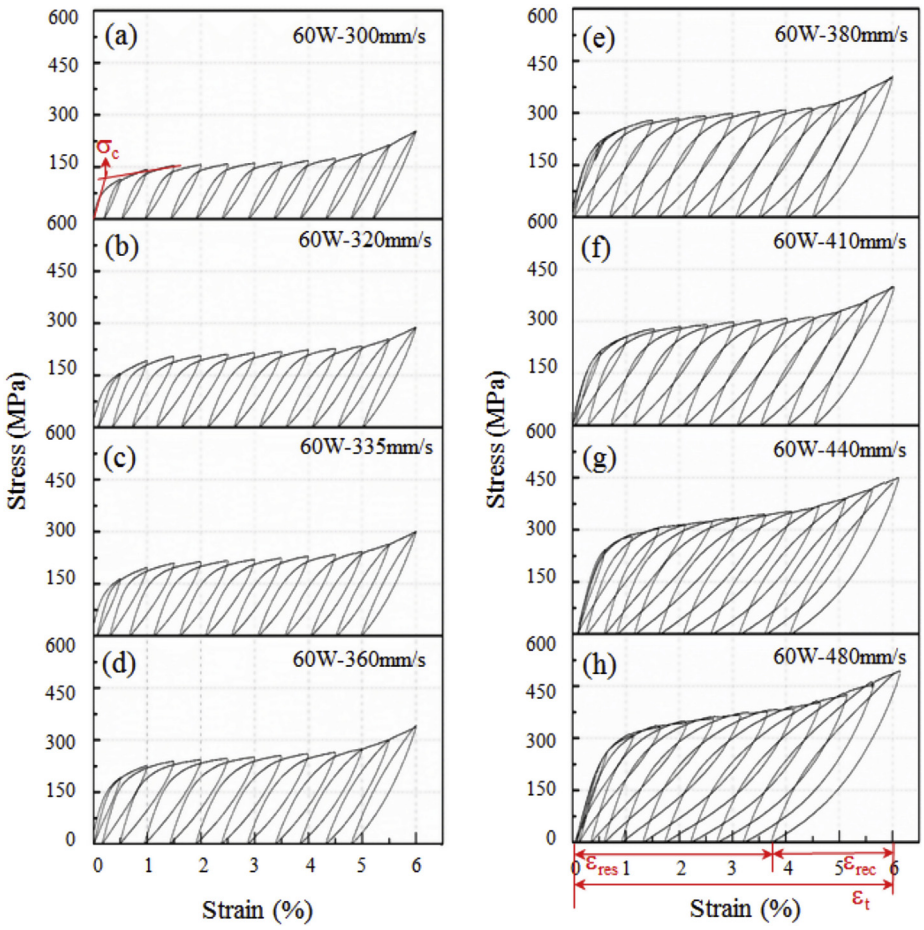

Fig. 7. Cyclic tensile curves till 6% strain of the SLM fabricated NiTi samples with different scanning speeds.

scanning speed. In general, the critical stress depends on the difference between M_s and testing temperature. As shown in Fig. 5b, once the testing temperature was settled as the room temperature for all samples, the lower M_s corresponding to the employment of a higher scanning speed leads to the higher critical stress. However, form the viewpoint of microstructure, the importance of the critical stress lies on its correspondence to the movement between adjacent martensitic B19′ plates or triggering the martensitic transformation from B2 phase to B19′ phase that normally depends on the initial phase constitution. As the driving force for relative movements between the pre-existing adjacent B19'/B19'interfaces are lower than the formation of the new B2/B19′ interface, the higher critical stress for sample fabricated with scanning speed of 480 mm/s than the 300 mm/s thus reflects that more volume fraction of B2 phase is contained for the former sample. Further, precipitates can also affect the critical stress for inducing martensitic transformation [31–34], but no precipitates was detected in the present samples with TEM. Therefore, the linear increase of critical stress for inducing martensitic transformation is in consistence with the decrease of M_s and the increase of volume fraction of B2 phase with the increasing of scanning speed.

The other value of mechanical recoverable strain was displayed in Fig. 8b. For the sample fabricated with scanning speed of 300 mm/s, the linear increase of mechanical recoverable strain due to the pure elastic deformation occurs before the applied strain is lower than 0.5%. For the sample fabricated with scanning speed of 360 mm/s, such a linear increase tendency is extended to the applied strain of approximate 1.0% which indeed exceeds the first yielding point in the tensile curve as shown in Fig. 7d. This is due to both the pure elastic deformation and the reversible stress-induced martensitic transformation. For the sample fabricated with the highest scanning speed of 480 mm/s, this linear stage is further extended to the higher applied strain of 2.5%. It can be observed from the corresponding tensile curved in Fig. 7h where the applied strain of 2.5% stands in the middle of the stress plateau. That suggests that the stress-induced martensitic transformation can largely reverse at a higher applied strain for this sample. Further, it can be observed that the mechanical recoverable strain is enhanced when the higher scanning speed is used. This is because that for the one fabricated with the low scanning speed of 300 mm/s, the recovery of the mechanical deformation is mainly attributed to the elastic recovery of the detwinned B19′ phase. While for the sample fabricated with the high scanning speed of 480 mm/s, partial B19′ phase would transform back to B2 phase during unloading, which leads to the increase of recoverable strain.

4.2. The evolution of functional properties with scanning speed

The evolution of functional properties (for example from shape memory effect to superelasticity) for the conventional NiTi alloy could be purposely adjusted via the change of testing temperature on loading. Indeed, in the present study, the evolution of functional properties occurs at the room temperature when the scanning speed solely increases while keeping the other processing parameters constant. In order to explore the relevant mechanisms for such evolution of functional properties with scanning speed,

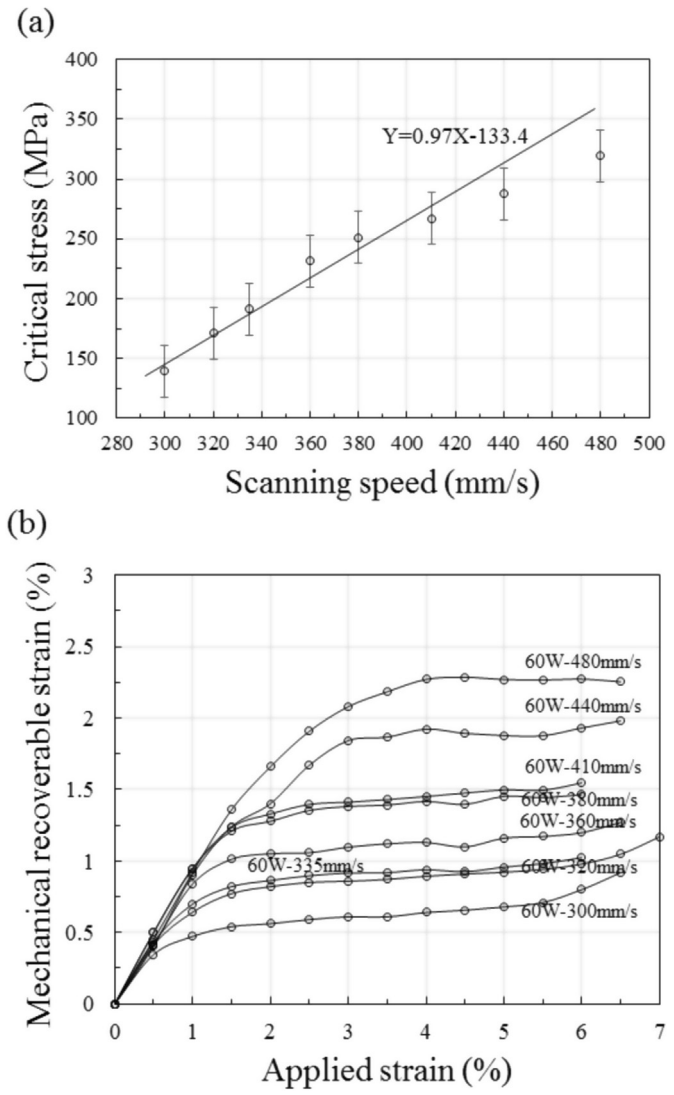

Fig. 8. (a) Evaluation of the critical stress for inducing martensitic transformation with increasing scanning speed and (b) mechanical recoverable strain with applied strain for the SLM fabricated NiTi alloy samples.

several factors including the chemical composition, initial phase constitution, crystallographic texture and microstructures are discussed.

The chemical composition for NiTi alloy is the most basic factor to modify the characteristic transformation temperature and further affect the initial phase constitution and functional properties. Taking the M_s temperature as an example, the relationship between the M_s and the Ni concentration for the forged NiTi alloy has already been investigated since last several tens of years, while the most prominent data available today (50 at. % < Ni < 51 at. %) was derived by Frenzel et al. and Tang et al. [35,36]. It was reported that the M_s is 333K for the equiatomic NiTi alloy, but it decreases with increasing Ni concentration by > 100K· at. $\%^{-1}$ when the composition value is located between 50 at. % and 51 at. %. Although the chemical composition for the present SLM fabricated NiTi alloy is not measured, the reduction of Ni content at higher laser power beam energy during SLM process has been accepted by most researches because the melting temperature for Ni (1455 °C) is indeed lower than the Ti (1668 °C) [16]. Whatever, the accurate chemical composition for the SLM fabricated NiTi alloy still deserves investigation in the future.

For the initial phase constitution, the relevant XRD results and microstructure in Figs. 2 and 3 and TEM observations in Figs. 5 and 6 demonstrate the co-existence of B2 and B19′ phases but no other precipitations. The decreased volume fraction of B19' phase corresponding to lower M_s temperature accounts for the increased critical stress and enhanced mechanical recoverable strain for sample fabricated with higher scanning speed. Regarding to the effect of dislocations, the density in Fig. 6 is not as high as in the cold deformed NiTi alloys. Indeed, the presence of dislocations could indeed strengthen the NiTi alloy and suppress the plastic deformation during B2−B19′ transformation, and an increase of the recoverable strain is expected. However, in this work, the samples fabricated with lower scanning speed show the higher dislocation density and lower recoverable strain. Therefore, it can be known that the dislocation density is not the main reason for the change of the recoverable strain.

The crystallographic texture for NiTi alloy is another important factor to affect the functional properties. This has already been well documented in conventional NiTi alloy for which, the most preferential orientation providing the maximum recoverable strain was experimentally and theoretically identified to be <111>$_{B2}$ orientation [30,37,38]. The PF in Fig. 4 indicated that the fiber texture of <111>//BD can be formed in all samples, but with increasing the scanning speed, the <100>//BD appears and all texture becomes weaken according to the discrete distribution of crystallographic orientation. This is probably due to the higher scanning speed cannot provide enough time for the preferential orientation to grow. Therefore, the slight difference on the texture variation with increasing scanning speed in the present study is not the key factor to be responsible for the evolution of functional properties.

In summary, the M_s temperature and initial phase constitution are the most important factor for the evolution of functional properties in the present case, while the variation of crystallographic texture and dislocation have limited influence. Indeed, the chemical composition analysis is the basic factor, hence a more persuasive static experimental results on a large number of samples fabricated with various parameters will be planned. In terms of the residual stress, it has never been investigated for the SLM fabricated NiTi alloy and indeed deserves deep investigation in the future.

5. Conclusion

The present work investigates the evolution of functional properties for the selective laser melting (SLM) fabricated NiTi alloy. The processing parameters of scanning speed from 300 mm/s to 480 mm/s under a constant laser power of 60 W were used to obtain different samples. The cyclic tensile test at room temperature was employed to evaluate the functional properties. The techniques of EBSD, TEM, XRD, textural detection, DSC were conducted to explore the relevant mechanisms. Some main conclusions can be drawn as follows.

(1) The microstructural observation were revealed by EBSD and TEM. It was shown that there is no apparent defects like the impurities and pore gas. The boundaries of columnar grains overlap apparently for the sample fabricated with the lowest scanning speed of 300 mm/s. The B2 phase was clearly identified by TEM for all sample tested samples, but the B19′ phase is difficult to be captured. The grain size of B2 is increased but the dislocation density is decreased with the scanning speed. No other precipitation was observed with TEM.

(2) The phase constitution was identified by XRD. Although the diffraction peaks of both B2 and B19′ phase were evident via

the peak separation and fitting processes, the volume fraction for each phase varies gradually amongst different samples. The volume fraction of B19′ phase becomes less with increasing the scanning speed and can be nearly neglected in the sample with the highest scanning speed of 480 mm/s.

(3) The crystallographic texture were measured with XRD. It was found that the <111>//BD texture was formed in three different samples fabricated with 300, 360 and 480 mm/s scanning speeds, respectively. But the <100>//BD texture only appears at relative higher scanning speed. Further, the higher scanning speed results to the more discrete distribution of crystallographic orientation.

(4) The cyclic tensile tests at room temperature were performed. The stress plateau and hysteresis loops relating with the martensitic transformation were observed for all samples. Two values which are the critical stress inducing martensitic transformation (σ_c) and the mechanical recoverable strain (ε_{rec}) were measured for further evaluation of the functional properties. The σ_c-ν shows a linear relationship with the slope of 0.97 MPa/mm.s^{-1}. The ε_{rec} - ε_t shows a linear increase firstly followed by a non-linear increase tendency and ends up with a plateau. The highest ε_{rec} of 2.29% was obtained for the sample fabricated with the highest scanning speed of 480 mm/s at the applied strain (ε_t) of 4.5%.

(5) The evolution of functional properties was confirmed with increasing scanning speed from the 300 mm/s to 480 mm/s for the SLM fabricated NiTi alloy samples. The variation of M_s temperature and initial phase constitution are the most two important factor to be responsible for this evolution of functional properties, while the variation of crystallographic texture and dislocation density have limited influence.

Acknowledgement

The work was financially supported by the National Natural Science Foundation of China for Young Scientists (grant numbers 51801199), by the National Key R&D Plan (grant number 2018YFB1105100) and by Scientific research foundation of advanced talents (innovation team), DGUT (No. KCYCXPT2016004).

References

[1] X. Wang, M. Speirs, S. Kustov, B. Vrancken, X. Li, J.-P. Kruth, J. Van Humbeeck, Selective laser melting produced layer-structured NiTi shape memory alloys with high damping properties and Elinvar effect, Scripta Mater. 146 (2018) 246–250.
[2] S. Saedi, N. Shayesteh Moghaddam, A. Amerinatanzi, M. Elahinia, H.E. Karaca, On the effects of selective laser melting process parameters on microstructure and thermomechanical response of Ni-rich NiTi, Acta Mater. 144 (2018) 552–560.
[3] S. Saedi, A.S. Turabi, M.T. Andani, C. Haberland, H. Karaca, M. Elahinia, The influence of heat treatment on the thermomechanical response of Ni-rich NiTi alloys manufactured by selective laser melting, J. Alloy. Comp. 677 (2016) 204–210.
[4] S. Dadbakhsh, B. Vrancken, J.P. Kruth, J. Luyten, J. Van Humbeeck, Texture and anisotropy in selective laser melting of NiTi alloy, Mater. Sci. Eng. A 650 (2016) 225–232.
[5] S. Saedi, A.S. Turabi, M.T. Andani, N.S. Moghaddam, M. Elahinia, H.E. Karaca, Texture, aging and superelasticity of selective laser melting fabricated Ni-rich NiTi alloys, Mater. Sci. Eng. A 686 (2017) 1–10.
[6] C. Haberland, H. Meier, J. Frenzel, On the properties of Ni-rich NiTi shape memory parts produced by selective laser melting, in: Proceedings of the ASME 2012 Conference on Smart Materials, Adaptive Structures and Intelligent Systems, American Society of Mechanical Engineers, 2012, pp. 97–104.
[7] S. Saedi, A.S. Turabi, M.T. Andani, C. Haberland, M. Elahinia, H. Karaca, Thermomechanical characterization of Ni-rich NiTi fabricated by selective laser melting, Smart Mater. Struct. 25 (2016) 035005.
[8] A. Bagheri, M.J. Mahtabi, N. Shamsaei, Fatigue behavior and cyclic deformation of additive manufactured NiTi, J. Mater. Process. Technol. 252 (2018) 440–453.
[9] M. Speirs, B. Van Hooreweder, J. Van Humbeeck, J.P. Kruth, Fatigue behaviour of NiTi shape memory alloy scaffolds produced by SLM, a unit cell design comparison, J. Mech. Behav. Biomed. Mater. 70 (2017) 53–59.
[10] M.T. Andani, S. Saedi, A.S. Turabi, M.R. Karamooz, C. Haberland, H.E. Karaca, M. Elahinia, Mechanical and shape memory properties of porous Ni50.1Ti49.9 alloys manufactured by selective lasermelting, J. Mech. Behav. Biomed. Mater. 68 (2017) 224–231.
[11] S. Dadbakhsh, M. Speirs, J. Kruth, J.V. Humbeeck, Influence of SLM on shape memory and compression behaviour of NiTi scaffolds, CIRP Ann. - Manuf. Technol. 64 (2015) 209–212.
[12] N.S. Moghaddam, S.E. Saghaian, A. Amerinatanzi, H. Ibrahim, P. Li, G.P. Toker, H.E. Karaca, M. Elahinia, Anisotropic tensile and actuation properties of NiTi fabricated with selective laser melting, Mater. Sci. Eng. A 724 (2018) 220–230.
[13] J. Sam, B. Franco, J. Ma, I. Karaman, A. Elwany, J.H. Mabe, Tensile actuation response of additively manufactured nickel-titanium shape memory alloys, Scripta Mater. 146 (2018) 164–168.
[14] B. Zhang, J. Chen, C. Coddet, Microstructure and transformation behavior of in-situ shape memory alloys by selective laser melting Ti–Ni mixed powder, J. Mater. Sci. Technol. 29 (2013) 863–867.
[15] M. Speirs, X. Wang, S.V. Baelen, A. Ahadi, S. Dadbakhsh, On the transformation behavior of NiTi shape-memory alloy produced by SLM, Shape Mem. Superelasticity 2 (2016) 310–316.
[16] X.B. Wang, S. Kustov, J.V. Humbeeck, A short review on the microstructure, transformation behavior and functional properties of NiTi shape memory alloys fabricated by selective laser melting, Materials 11 (2018) 1683.
[17] T. Bormann, B. Müller, M. Schinhammer, A. Kessler, P. Thalmann, M.de Wild, Microstructure of selective laser melted nickel-titanium, Mater. Char. 94 (2014) 189–202.
[18] Y. Yang, J.B. Zhan, B. Li, J.X. Lin, J.J. Gao, Z.Q. Zhang, L. Ren, P. Castany, T. Gloriant, Laser beam energy dependence of martensitic transformation in SLM fabricated NiTi shape memory alloy, Materialia 6 (2019) 100305.
[19] L. Thijs, F. Verhaeghe, T. Craeghs, J.V. Humbeeck, J.-P. Kruth, A study of the microstructural evolution during selective laser melting of Ti-6Al-4V, Acta Mater. 58 (2010) 3303–3312.
[20] L.C. Zhang, Y. Liu, S. Li, Y. Hao, Additive manufacturing of titanium alloys by electron beam melting: a review, Adv. Eng. Mater. 20 (2018) 1700842.
[21] Y.J. Liu, S.J. Li, H.L. Wang, W.T. Hou, Y.L. Hao, R. Yang, T.B. Sercombe, L.C. Zhang, Microstructure, defects and mechanical behavior of beta-type titanium porous structures manufactured by electron beam melting and selective laser melting, Acta Mater. 113 (2016) 56–67.
[22] X. Zhou, K. Li, D. Zhang, X. Liu, J. Ma, W. Liu, Z. Shen, Textures formed in a CoCrMo alloy by selective laser melting, J. Alloy. Comp. 631 (2015) 153–164.
[23] A. Takaichi, Suyalatu, T. Nakamoto, N. Joko, N. Nomura, Y. Tsutsumi, S. Mijita, H. Doi, S. Kurosu, A. Chiba, N. Wakabayashi, Y. Igarashi, T. Hanawa, Microstructures and mechanical properties of Co–29Cr–6Mo alloy fabricated by selective laser melting process for dental applications, J. Mech. Behav. Biomed. Mater. 21 (2013) 67–76.
[24] L. Thijs, K. Kempen, J.-P. Kruth, J. Van Humbeeck, Fine-structured aluminium products with controllable texture by selective laser melting of pre-alloyed AlSi10Mg powder, Acta Mater. 61 (2013) 1809–1819.
[25] L.N. Carter, C. Martin, P.J. Withers, M.M. Attallah, The influence of the laser scan strategy on grain structure and cracking behaviour in SLM powder-bed fabricated nickel superalloy, J. Alloy. Comp. 615 (2014) 338–347.
[26] M. Simonelli, Y.Y. Tse, C. Tuck, On the texture formation of selective laser melted Ti-6Al-4V, Metall. Mater. Trans. A 45 (2014) 2863–2872.
[27] H.C. Lin, S.K. Wu, J.C. Lin, The martensitic transformation in Ti-rich TiNi shape memory alloys, Mater. Chem. Phys. 37 (1994) 184–190.
[28] J. Khalil-Allafi, B. Amin-Ahmadi, Multiple-step martensitic transformations in the Ni51Ti49 single crystal, J. Mater. Sci. 45 (2010) 6440–6445.
[29] G. Lütjering, J.C. Williams, Titanium, second ed., Springer-Verlag, Berlin, 2007, p. 141.
[30] K. Otsuka, X. Ren, Physical metallurgy of Ti-Ni-based shape memory alloys, Prog. Mater. Sci. 50 (2005), 511-678.
[31] X.B. Wang, S. Kustov, K. Li, D. Schryvers, B. Verlinden, J.V. Humbeeck, Effect of nanoprecipitates on the transformation behavior and functional properties of a Ti-50.8 at. % Ni alloy with micron-sized grains, Acta Mater. 82 (2015) 224–233.
[32] K. Ga, H.J. Maier, Cyclic deformation mechanisms in precipitated NiTi shape memory alloys, Acta Mater. 50 (2002) 4643–4657.
[33] R.F. Zhu, J.N. Liu, G.Y. Tang, S.Q. Shi, M.W. Fu, T.S.E. Zion Tsz Ho, The improved superelasticity of NiTi alloy via electropulsing treatment for minutes, J. Alloy. Comp. 584 (2014) 225–231.
[34] S. Barbarino, E.I. Saavedra Flores, R.M. Ajaj, I. Dayyani, M.I. Friswell, Topical Review: a review on shape memory alloys with applications to morphing aircraft, Smart Mater. Struct. 23 (2014) 063001.
[35] Transformation in the Ti-Ni system, Acta Mater. 47 (1999) 3457–3468.
[36] J. Frenzel, E.P. George, A. Dlouhy, Ch Somsen, M.F.-X. Wagner, G. Eggeler, Influence of Ni on martensitic phase transformations in NiTi shape memory alloys, Acta Mater. 58 (2010) 3444–3458.
[37] P. Zhang, M. Zhu, L. Wang, C. Li, Q. Zhai, Investigation on microstructure and memory property of NiTi single crystal shape memory alloys, Rare Metal Mater. Eng. 39 (2010) 762–766.
[38] G. Laplanche, J. Pfetzing-Micklich, G. Eggeler, Orientation dependence of stress-induced martensite formation during nanoindentation in NiTi shape memory alloys, Acta Mater. 68 (2014) 19–31.